

Multi-scale Context-aware Network with Transformer for Gait Recognition

Duowang Zhu, Xiaohu Huang, Xinggang Wang, Bo Yang, Botao He, Wenyu Liu, and Bin Feng

Abstract—Although gait recognition has drawn increasing research attention recently, since the silhouette differences are quite subtle in spatial domain, temporal feature representation is crucial for gait recognition. Inspired by the observation that humans can distinguish gaits of different subjects by adaptively focusing on clips of varying time scales, we propose a multi-scale context-aware network with transformer (MCAT) for gait recognition. MCAT generates temporal features across three scales, and adaptively aggregates them using contextual information from both local and global perspectives. Specifically, MCAT contains an adaptive temporal aggregation (ATA) module that performs local relation modeling followed by global relation modeling to fuse the multi-scale features. Besides, in order to remedy the spatial feature corruption resulting from temporal operations, MCAT incorporates a salient spatial feature learning (SSFL) module to select groups of discriminative spatial features. Extensive experiments conducted on three datasets demonstrate the state-of-the-art performance. Concretely, we achieve rank-1 accuracies of 98.7%, 96.2% and 88.7% under normal-walking, bag-carrying and coat-wearing conditions on CASIA-B, 97.5% on OU-MVLP and 50.6% on GREW. The source code will be available at <https://github.com/zhuduowang/MCAT.git>.

Index Terms—Gait Recognition, Temporal Relation Modeling, Spatial Feature Preserving.

I. INTRODUCTION

GAIT recognition is a biometric technology that identifies individuals based on their walking patterns. It has shown great potential in applications related to public security [1]–[4] and identity recognition [5]–[7]. Despite the increasing research attention on gait recognition, learning temporal feature representation is crucial due to the subtle differences in the spatial domain.

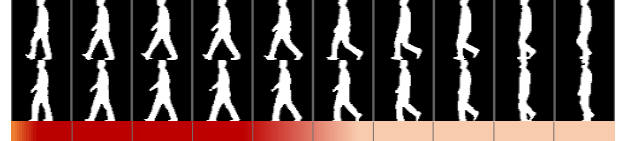
Furthermore, as mentioned in [8], different body parts exhibit varied motion patterns, thus require temporal modeling to take multi-scale representation into consideration. Currently, multi-layer convolutions are commonly utilized in current methods to model multi-scale temporal information. These methods aggregate multi-scale features through summation [8]–[11], or concatenation [12], [13]. However, these fixed aggregation methods lack the flexibility to adapt to variations of complex motion and realistic factors, i.e., self occlusion between body parts and changes in camera viewpoints. Consequently, this limitation hinders the performance, particularly

Duowang Zhu, Xiaohu Huang, Xinggang Wang, Wenyu Liu and Bin Feng are with the Hubei Key Laboratory of Smart Internet Technology, and also with the School of Electronic Information and Communications, Huazhong University of Science and Technology, Wuhan 430074, China.

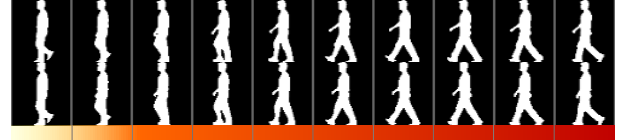
Bo Yang is with Wuhan FiberHome Digital Technology Co., Ltd. And Botao He is with CICT Mobile Communication Technology Company Ltd.

Duowang Zhu and Xiaohu Huang contributed equally to this work.

Bin Feng (fengbin@hust.edu.cn) is the corresponding author.



(a) Two sequences from subject '53' and '119' on CASIA-B can be distinguished relying on short-term temporal clues, e.g., several frames at the beginning.



(b) Two sequences from subject '39' and '77' on CASIA-B, which have to be distinguished relying on long-term temporal clues, e.g., all of the frames.

Fig. 1. Illustration that humans are capable of distinguishing gaits of different subjects by adaptively focusing on temporal fragments with different time scales. Color bar indicates the distribution of human attention. Darker color represents a higher level of attention paid to corresponding frames. Best viewed in color.

considering that gait is a kind of fine-grained motion pattern, and subject identification relies on the varied expression of customized motion on specific body parts.

It can be seen from life experience that human is able to distinguish gait sequences of different subjects by selectively attending to temporal fragments characterized by distinct time scales. A qualitative illustration is given in Figure. 1, where voting results from 15 volunteers are used to calculate the focus distribution. In Figure. 1(a), the differences between the two gait sequences are so obvious that we can distinguish them by observing fewer frames from the beginning. On the contrary, in Figure. 1(b), differences between two sequences are quite subtle that we have to observe more frames to distinguish them. Therefore, in this situation, relying solely on short-term clues is inadequate for distinguishing between the two subjects, but long-term features need to be considered since they provide richer temporal information. Consequently, the adaptation of multi-scale temporal features facilitates a flexible focus along the temporal dimension, thereby providing a novel perspective for gait modeling.

Motivated by such observations, we propose a Multi-scale Context-aware Network with Transformer (MCAT) for gait recognition. The core idea of this method is to integrate multi-scale temporal features by considering the contextual information along temporal dimension, which allows information exchange among different scales from both local and global perspectives. Here, contextual information is obtained by evaluating the local and global relations among multi-scale

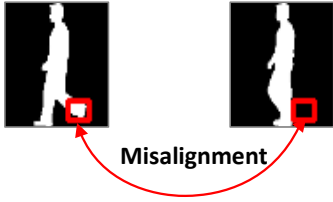


Fig. 2. Illustration of the misalignment in gait sequences. Since pixels of the same spatial locations in different frames may correspond to different semantic contents, the utilization of temporal operations could lead to blurred or overlapped appearances.

temporal features, which reflects diverse motion information existing in context semantics. MCAT produces temporal features for each frame in three scales, i.e., frame-level, short-term and long-term, which are complementary to each other. The frame-level features retain frame characteristics at each time instant. The short-term features capture local temporal contextual clues, which are sensitive to temporal locations and contribute to model micro motion patterns. The long-term features, representing motion characteristics across all frames, reveal global action periodicity and remain invariant to temporal locations.

Next, a local relation modeling among these temporal features guides the network to adaptively enhance or suppress temporal features with different scales in each frame. Afterwards, a global relation modeling is involved to interact the multi-scale features along the whole sequence, constructing global communication to capture the most discriminative representation. Inspired by some recent works [14]–[18] that use Transformer [19] to improve the model’s ability to learn global relations, we adopt a Transformer block to model global relations across multi-scale features. Our method forms a hierarchical framework to adaptively aggregate multi-scale features in both local and global aspects, allowing for the modeling of complex motion and making it highly suitable for gait recognition.

Furthermore, we notice a misalignment problem in the temporal modeling of gait recognition that has not yet been explored. As shown in Figure. 2, the same pixel locations from different frames may correspond to different foregrounds and backgrounds. The utilization of temporal operations, such as temporal convolution and temporal pooling, naturally leads to blurry and corrupted appearances. However, appearance features could provide some auxiliary information for distinguishing different people. To address such issue, we propose a salient spatial feature learning (SSFL) module to select discriminative local spatial parts across the whole sequence, which can be considered as supplements to remedy the corruption in appearance features. The discriminative feature selection relies on evaluating the importance of temporal features, for which we employ the multi-head self-attention (MHSA) mechanism to generate groups of global importance maps. In particular, as described in [19], each head concentrates on a specific representation subspace, enabling multiple heads to generate diverse importance maps. These maps enable the selection of groups of discriminative local components from

various perspectives.

The adaptive temporal modeling and salient spatial learning provide complementary properties for each other. On one hand, adaptive temporal aggregation (ATA) module mainly considers temporal modeling and salient spatial feature learning (SSFL) module focuses on spatial learning. Specifically, ATA produces temporal aggregation of multi-scale clues which describes motion patterns, and SSFL selects well-preserved spatial features based on saliency evaluations, which are related to static images. On the other hand, MCAT aggregates temporal clues in a soft-attention way and SSFL obtains salient spatial features in a hard-attention manner. In a nutshell, by jointly investigating motion learning and spatial mining simultaneously, we achieve outstanding performance over the state-of-the-art methods.

The main contributions of the proposed method are summarized as the following three aspects:

- In this paper, we propose a temporal modeling network MCAT to fuse multi-scale temporal features in an adaptive way from both local and global aspects, which considers the cross-scale contextual information as a guidance for temporal aggregation.
- We propose a salient spatial feature learning (SSFL) module to remedy the feature corruption caused by temporal operations. SSFL constructs global feature importance maps to select salient spatial features across the whole sequence, which provide high quality spatial clues.
- Extensive experiments conducted on three datasets, i.e., CASIA-B [20], OU-MVLP [21] and GREW [22], demonstrate the state-of-the-art performance of MCAT. And further ablation experiments prove the effectiveness of the proposed modules. Additional experiments using practical settings reveal the real-world application potentials of MCAT.

A preliminary conference version of this work was published in ICCV-2021 [23]. We make three improvements to this work: (1) We extend the adaptive multi-scale feature aggregation from a local approach to a hierarchical approach that encompasses both local and global scales. This modification results in improved recognition performance. (2) The former SSFL constructs importance maps on each frame individually, and only generates a group of salient parts. Instead, the improved SSFL forms the importance maps in a global view by utilizing the multi-head self-attention mechanism, which is capable of generating more groups of salient spatial parts, thereby enhancing spatial mining capacity. (3) We conduct additional experiments on a recently published large-scale gait dataset captured in the wild, i.e., GREW [22], on which we further validate the effectiveness and robustness of our method. And more ablation experiments are conducted on CASIA-B to analyze the contribution of the proposed modules, explore the network design, and study the performances of our method in simulated real-world scenarios.

The rest of this paper is organized as follows. Firstly, the Section II describes the related work. Next, the Section. III gives the details of the proposed method. Afterwards, the Section. IV provides comprehensive experiments and corre-

sponding analysis. Finally, the Section. V concludes the paper and present future work.

II. RELATED WORK

A. Gait Recognition

Current gait recognition methods could be categorized into two types: model-based and appearance-based.

Model-based methods [?], [25]–[27] were proposed to model walking patterns and body structures of humans based on extracted key points [28]–[30]. Model-based methods are robust to variations of clothing and camera viewpoints. However, due to (1) inaccurate pose results estimated from low-quality images and (2) the missing of identity-related shape information, model-based methods are usually inferior to appearance-based methods in performance comparison.

Appearance-based methods [8], [10], [12], [31]–[37] extracted spatio-temporal features binary silhouettes by CNN networks or handcrafted algorithms. Gait Energy Image (GEI) [34] was generated through projecting a sequence of gait silhouettes into a single image. The GEI-based methods [34]–[39] greatly compressed computational cost but lost discriminative expression. In contrast, the video-based approaches [8], [10]–[13], [31], [32], [40]–[42] processed gait sequences frame by frame, which maintained the frame-level discriminative feature in a large extent, and benefited the networks to learn temporal representation. Our approach belongs to appearance-based method and takes silhouette sequences as input.

B. Temporal Modeling

Current literatures proposed different strategies for gait temporal modeling, including 1D convolutions, LSTMs and 3D convolutions etc. Particularly, GaitSet [31], GLN [32] and GaitBase [43] considered a gait sequence as an unordered set, which mainly focused on spatial modeling and captured inter-frame dependency implicitly. GaitPart [8] and Wu et al. [9] extracted local temporal clues by convolutions and aggregated them in a summation or a concatenation manner. LSTM networks were applied in [10], [11] to achieve long-short temporal modeling, which fused temporal clues by temporal accumulation. With the help of stacked 3D blocks, MT3D [12] and GaitGL [13] incorporated temporal information with small and large scales, then concatenated or summed these features as outputs. 3DLocal [44] applied 3D CNN to obtain different local parts, and fused them with feature concatenation. GaitTransformer [41] proposed Multiple-Temporal-Scale Transformer (MTST) module to model the long-term features. However, current methods have obvious shortcomings in learning flexible and robust multi-scale temporal features, which are incapable of satisfying temporal modeling requirements for different body parts of gait motion.

Recently, transformers were broadly applied in various computer vision tasks [45]–[48]. Compared with the prevalent CNNs, the most outstanding strength of transformers is the global reasoning capacity, which empowers models to capture features in the long range. In the domain of video-based tasks, TPT [49], ViViT [50] and Vidtr [51] proved transformers could extract global temporal features effectively.

Our method differs from above methods in three aspects: (1) MCAT generates temporal features in three scales, i.e., frame-level, short-term and long-term. Such rich temporal clues enable our network to obtain diverse motion learning ability. (2) For fusing multi-scale temporal features adaptively, MCAT employs both local and global cross-scale relation modelings to obtain the most appropriate temporal expression. (3) The transformer block we use is not for global feature extraction like current methods, but for global feature interaction on multiple time scales.

C. Spatial Preserving

The spatial appearance features provide supplementary cues to recognize people besides motion pattern. GaitNet [11] proposed a disentanglement-based scheme to obtain the canonical feature to help recognition, whose goal was close to ours. Except for gait recognition, the spatial misalignment also degraded performance in other person-related recognition task, e.g. Person Re-identification. In video-based Person Re-identification, different methods were proposed to maintain the clearness of spatial features. In AP3D [52], researchers proposed Appearance Preserving Module (APM) to mitigate the misalignment problem in temporal modeling. APM used a feature similarity calculation strategy to match the foregrounds in continuous frames within a local window based on the color, texture and illumination et al. Chen et al. [53] proposed a method dubbed Adversarial Feature Augmentation (AFA) to capture motion coherence by a adversarial form. However, AFA only employed motion-irrelevant features, but totally abandoned temporal clues.

Unfortunately, the above spatial preserving methods are not appropriate for gait recognition. GaitNet and APM are both operated on RGB-based appearance features, e.g., color, texture and illumination. But the inputs of our model are sequences of binary silhouettes, which do not include the needed appearance features. Moreover, AFA only incorporated the modeling of motion-irrelevant features but ignored the motion-relevant features, which are vital for gait recognition.

Different from these strategies, in our approach, SSFL selects discriminative local parts to maintain the spatial characteristics of subjects, which is feasible for binary inputs. And this operation is parallel to temporal modeling, thus would not compromise temporal feature extraction.

III. PROPOSED METHOD

In this section, we firstly describe the overall pipeline of our method, then illustrate the detailed structure of key components in the network.

A. Overall Architecture

The overview structure of our method is presented in Figure. 3. A batch of B gait samples of N frames are fed into the network as input, which is denoted as $G \in \mathbb{R}^{B \times N \times H \times W}$ where H and W denote the height and width of each frame respectively. Firstly, G is passed through a 2D CNN to extract spatial feature $F_I \in \mathbb{R}^{B \times N \times C \times H/2 \times W/2}$, where C

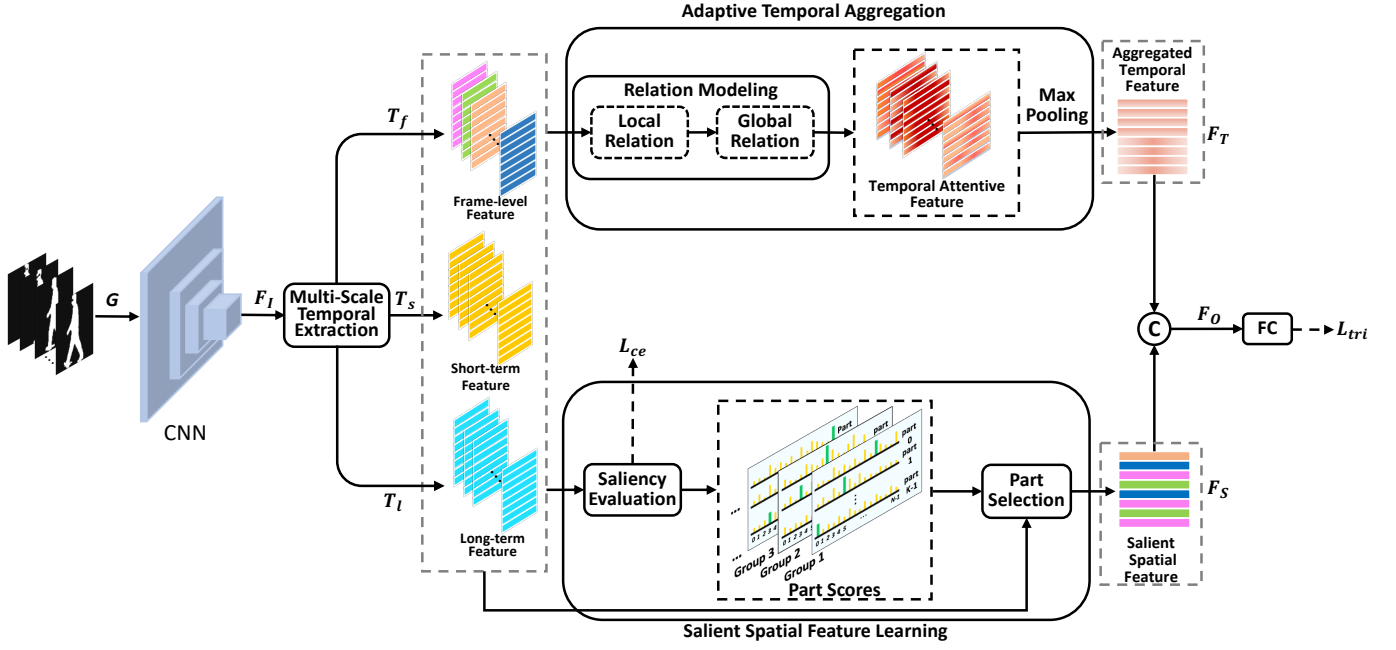


Fig. 3. Overview of MCAT. A sequence of gait silhouettes are firstly fed into a 2D CNN to extract spatial features in each frame. Then, a multi-scale temporal extraction (MSTE) module is utilized to obtain temporal features in three scales. Afterwards, a two-branch architecture composed of an adaptive temporal aggregation (ATA) module and a salient spatial feature learning (SSFL) module is formed to aggregate multi-scale features and select salient spatial parts respectively. Arrows, G , F_I , F_T , F_S and F_O denote operations, input gait sequence, features processed by CNN, temporal aggregated features, salient spatial features and output features respectively. L_{tri} and L_{ce} represent triplet loss and cross-entropy loss respectively.

denotes the number of feature channels. The detailed CNN architecture is given in Table. I. Afterwards, we implement a multi-scale temporal extraction (MSTE) module on F_I to generate temporal features with three different temporal scales, i.e., frame-level, short-term and long-term, which are denoted as T_f , T_s and T_l respectively. T_f , T_s and T_l are all with size of $\mathbb{R}^{B \times N \times C \times K}$, where K denotes the number of horizontal divided feature parts that correspond to body parts in some extent. Next, temporal features are fed into adaptive temporal aggregation (ATA) and salient spatial feature learning (SSFL) blocks respectively, through which we obtain temporal aggregated feature $F_T \in \mathbb{R}^{B \times C \times K}$ and salient spatial feature $F_S \in \mathbb{R}^{B \times C \times K}$ correspondingly. Temporal aggregated feature F_T is a temporal summarization of the whole sequence, which represents the discriminative information in temporal domain. Spatial salient feature F_S is obtained by selecting groups of salient spatial parts, which maintain rich high-quality silhouette information. Finally, F_S and F_T are concatenated along channel dimension as outputs F_O .

TABLE I
STRUCTURE OF THE BACKBONE ON CASIA-B. C_{in} AND C_{out} DENOTE THE INPUT CHANNEL AND OUTPUT CHANNEL OF EACH LAYER RESPECTIVELY.

Layer	C_{in}	C_{out}	Kernel	Pad	Activation
Conv1	1	32	3	1	Leaky ReLU
Conv2	32	64	3	1	Leaky ReLU
	Max Pooling kernel=(2,2), stride=2				
Conv3	64	128	3	1	Leaky ReLU
Conv4	128	128	3	1	Leaky ReLU

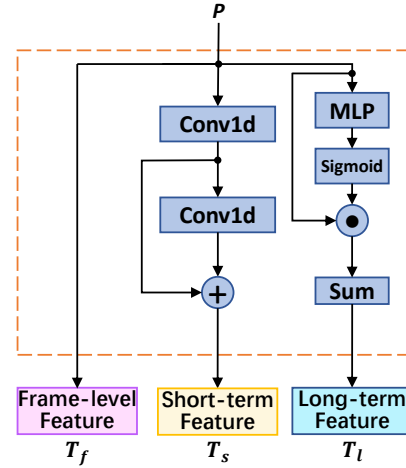


Fig. 4. Detailed architecture of Multi-Scale Temporal Extraction, which produces temporal features in three levels for each frame.

B. Multi-Scale Temporal Extraction

As discussed in Section. III-A, we aim to enrich the diversity of temporal features. Firstly, we divide F_I into K parts vertically, then apply Global Max Pooling (GMP) and Global Average Pooling (GAP) to obtain part-level pooling features $P \in \mathbb{R}^{B \times N \times C \times K}$, where $P^{b,n}$ represents part-level features of the n -th frame in the b -th sample. As shown in Figure. 4, the frame-level features are the duplicate of P , which do not get involved with temporal operation, thus the appearance characteristics of each time instant are well-maintained.

In order to capture short-term temporal features, we apply

two serial 1D convolutions with kernel size of 3, and add the features after each 1D convolution as T_s . Obtaining short-term features enables the network to focus on short period temporal motion patterns and subtle changes with perceptive fields of 3 and 5.

The long-term feature extraction is based on the combination of all frames. Firstly, a Multi-layer Perceptron (MLP) followed by a Sigmoid function is applied on P to evaluate the importance of different frames. Next, the weighted summation of all frames by the importance scores is utilized as the long-term temporal features T_l , which is formulated as:

$$T_l^b = \frac{\sum_{n=1}^N \text{Sigmoid}(\text{MLP}(P^{b,n})) \odot P^{b,n}}{\sum_{n=1}^N \text{Sigmoid}(\text{MLP}(P^{b,n}))}, \quad (1)$$

where \odot denotes dot product. It should be noted that, T_l^b is invariant for all frames in the b -th sample, which describes global motion cues. After that, we obtain temporal features of three levels, e.g., T_f , T_s and T_l , for subsequent ATA and SSFL blocks.

C. Adaptive Temporal Aggregation

In this part, we utilize multi-scale temporal features to explore feature relations, which enable information exchanging among different temporal scales. As discussed in [8], different body parts own various motion patterns, which indicates the diverse expressions are needed for temporal modeling. Intuitively, as shown in Figure. 5, the interaction of different scales of features would effectively enrich the diversity of temporal representation, thus produce suitable motion expression for human body. As stated in Section. I, the feature interactions are conducted both locally and globally, which are illustrated below.

1) *Local Relation Modeling*: In order to achieve local aggregation in each frame, we concatenate the features from three scales along the channel dimension. Then we take a fully-connected (FC) layer to correlate the channels and obtain the fused output, which is represented as:

$$T_{A_l}^{b,n} = \text{FC}(T_f^{b,n} \odot T_s^{b,n} \odot T_l^{b,n}), \quad (2)$$

where \odot denotes the concatenation operation and FC is a 1D depth-wise convolutions with kernel size of 1.

Subsequently, the local aggregated feature T_{A_l} is utilized as input to the global relation modeling module.

2) *Global Relation Modeling*: To achieve global interactions, we use transformer to construct multi-scale relation modeling across the whole sequence. As discussed in [19], [45], [46], position encoding (PE) plays an important role to achieve permutation-variant modeling in transformers. Considering the various lengths of gait sequences, we adopt conditional position encoding [54] to extract PE, which can fit the sequence length adaptively. As shown in Figure. 5(b), PE is obtained by applying 1D depth-wise convolutions with kernel size of 3 on T_{A_l} , which produces feature $T_{trans} \in \mathbb{R}^{B \times K \times N \times C}$. Following [19], we first apply a layer normalization on T_{trans} and then conduct three feature transformations

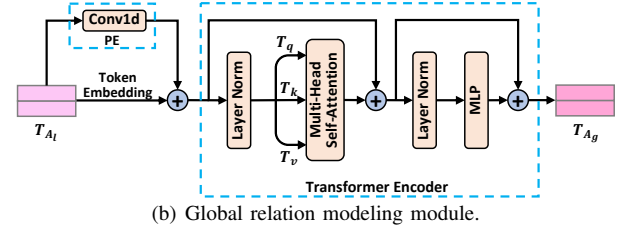
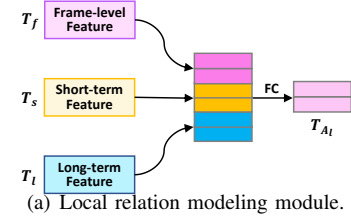


Fig. 5. The detailed structure for modeling local-global relations between multi-scale features.

with three learnable matrix weights W_q , W_k and W_v , which are formulated as:

$$T_{norm} = \text{Norm}(T_{trans}) \quad (3)$$

$$T_q = T_{norm}W_q, \quad T_k = T_{norm}W_k, \quad T_v = T_{norm}W_v, \quad (4)$$

where W_q , W_k and W_v are all with the dimension of $N_{head} \times C \times C/N_{head}$, and N_{head} denotes the number of heads. Then, the attention matrix is obtained by multiplying T_q with T_k followed by a Softmax normalization:

$$A_T = \text{Softmax}(T_q T_k / \sqrt{C}), \quad (5)$$

where $A_T \in \mathbb{R}^{B \times N_{head} \times K \times N \times N}$ and \sqrt{C} is used to normalize the dot-product scores. Afterwards, we utilize the attention matrix A_T to generate attentive feature T_a with a shortcut and a normalization layer:

$$T_a = A_T T_v + T_{trans}, \quad (6)$$

where $T_a \in \mathbb{R}^{B \times K \times N \times C}$. Subsequently, we use a layer normalization and a feed-forward network (FFN) [19], such as MLP, to obtain the globally fused multi-scale feature T_{A_g} :

$$T_{A_g} = \text{FFN}(\text{Norm}(T_a)) + T_a, \quad (7)$$

where $T_{A_g} \in \mathbb{R}^{B \times K \times N \times C}$. Finally, a max pooling along temporal dimension is applied on T_{A_g} to obtain sequence-level temporal representation $F_T \in \mathbb{R}^{B \times K \times C}$.

D. Salient Spatial Feature Learning

In this section, we aim to extract salient spatial parts to mitigate the damage in appearance features.

1) *Discussion*: Intuitively, in order to remedy the corrupted spatial features, we should select an individual frame as the methods in [55], [56], which is illustrated in Figure. 6(a). However, due to the various camera viewpoints, motion occlusions and imperfect segmentations, a single frame is probably incapable of expressing appearance features for all body parts clearly. Actually, the high quality body parts appear and disappear from frame to frame. Therefore, by utilizing such inherent motion characteristics, we select salient body

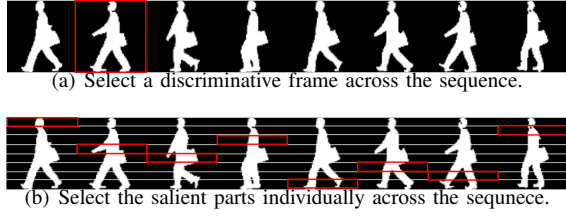


Fig. 6. Illustration of two ways to select salient spatial features. Compared with selecting a frame, selecting the salient parts is conducted in a more fine-grained level, thus could obtain more high-quality local features.

parts across the whole sequence. As shown in Figure. 6(b), we obtain local discriminative features in different frames instead of directly selecting one frame.

Since the transformer is able to correlate global information based on the attention matrix adaptively, the weights in the attention matrix could reveal feature importance in some extent. Naturally, a body part that contains clearer feature representation has a stronger weight than a body part with vague feature representation. Therefore, we consider using the attention matrix as a metric to select salient spatial parts. Besides, due to the diversities in multiple heads [19], attention matrices in different heads may focus on informative features from various aspects, which enhances the spatial mining capacity.

2) *Operation*: Considering temporal clues provide contextual information for evaluating the discrimination of each frame, we firstly utilize a FC to fuse the multi-scale features. Then, we construct the attention matrix $A_s \in \mathbb{R}^{B \times N_{head} \times K \times N \times N}$ as in Equation. 4 and Equation. 5, but remove the scale operation and Softmax function. Next, we squeeze the attention matrix along the column dimension, which is formulated as:

$$\tilde{A}_s^{b, :, :, :} = \sum_{n=1}^N A_s^{b, :, :, :, n}, \quad (8)$$

where $\tilde{A}_s^{b, :, :, :} \in \mathbb{R}^{N_{head} \times K \times N}$ denotes the part scores of K parts from N_{head} heads in the b -th sample. The values of part scores represent feature importance, thus higher scores indicate clearer spatial representation. In order to supervise the correctness of part scores, we enforce a cross-entropy loss on the weighted summation of T_f and \tilde{A}_s . Here, the weighted feature F_w is obtained by:

$$F_w^b = \sum_{n=1}^N T_f^{b, n} \odot \tilde{A}_s^{b, :, :, n}, \quad (9)$$

where $F_w^b \in \mathbb{R}^{N_{head} \times K \times C}$ of the b -th sample. Then, a FC layer is utilized to transform F_w into classification logics $P_w \in \mathbb{R}^{B \times N_{head} \times K \times C_t}$, where C_t denotes the number of training subjects. Afterwards, the cross-entropy loss is applied on P_w to produce L_{ce} :

$$L_{ce} = - \sum_{b=1}^B \sum_{h=1}^{N_{head}} \sum_{c=1}^{C_t} y_{b,c} \log(\text{SoftMax}(P_w^{b,h}))_c, \quad (10)$$

where $y_{b,c}$ indicates the identity information of the b -th sample, which equals 0 or 1. Next, we obtain part indexes of the highest scores along temporal dimension:

$$x^{b,h,k} = \arg \max_n \tilde{A}_s^{b,h,k,n}, \quad (11)$$

where $x^{b,h,k}$ denotes the temporal index of the selected k -th part in the h -th head of the b -th sample. By using the index $\{x^{b,h,k} | k = 1, 2, \dots, K\}$ in a hard-attention manner, we obtain the recombinant frame feature F_r in the h -th head of the b -th sample:

$$F_r^{b,h} = T_f^{b,x^{b,h,1}} \odot T_f^{b,x^{b,h,2}} \cdots \odot T_f^{b,x^{b,h,K}}, \quad (12)$$

where \odot denotes concatenation along part dimension. In the end, we fuse the recombinant features F_r with the weighted features F_w in different heads by:

$$F_S^b = \left(\sum_{h=1}^{N_{head}} F_r^{b,h} \right) \odot \left(\sum_{h=1}^{N_{head}} F_w^{b,h} \right), \quad (13)$$

where $F_S^b \in \mathbb{R}^{K \times C}$ denotes the obtained salient spatial features of the b -th sample, and \odot denotes channel concatenation. F_S offers supplementary spatial clues for temporal aggregated features F_T . Triplet loss [57] is employed on the combination of F_S and F_T as metric learning loss function. The overall loss function is presented as following:

$$L = L_{ce} + L_{tri} \quad (14)$$

IV. EXPERIMENTS AND DISCUSSION

A. Datasets and Evaluation Metrics

We conduct experiments on three standard datasets, i.e., CASIA-B [20], OU-MVLP [21] and GREW [22], to verify the superiority of our method. Further ablation experiments are conducted on CASIA-B to demonstrate the positive impact of each component in our method.

CASIA-B. CASIA-B [20] is composed of 124 subjects, and each subject contains 110 sequences with 11 different camera views. Under each camera view, every subject contains three walking conditions, i.e., normal (NM) (6 sequences), walking with bag (BG) (2 sequences) and walking with coat (CL) (2 sequences). For the training and testing stages, we follow the protocols in [36]. The samples from the first 74 subjects are considered as training set, and the remaining 50 subjects are considered as test set. At testing phase, the first 4 sequences in NM condition of each subject are regarded as gallery set and the remaining 6 sequences of each subject are used as probe set, including 2 sequences of NM, 2 sequences of BG and 2 sequences of CL.

OU-MVLP. OU-MVLP [21] is composed of 10307 subjects. Each subject contains 28 sequences with 14 camera views, thus each subject contains 2 sequences (index '01' and '02') for each view. The first 5153 subjects are used for training, while the remaining 5154 subjects are for testing. In particular, the sequences with index '01' are regarded as gallery and the sequences with index '02' are regarded as probe set at testing phase.

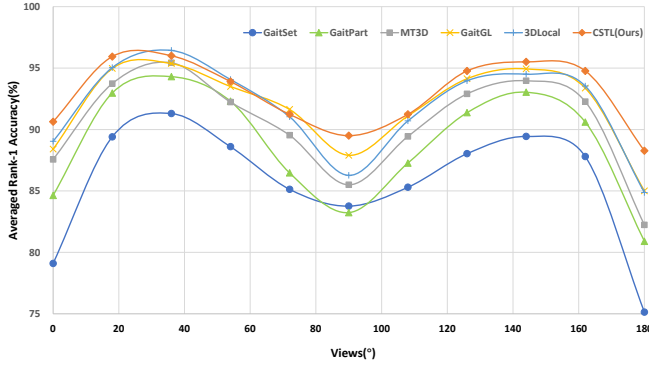


Fig. 7. Multi-view performance comparison on CASIA-B using curve chart, in terms of averaged rank-1 accuracy.

GREW. GREW [21] captures gait videos under uncontrolled conditions, which is composed of 26345 subjects and, 128671 sequences in total. In particular, 882 cameras are involved to record the videos, where the corresponding views are not predefined like CASIA-B or OU-MVLP. Concretely, the training set includes 102887 sequences of 20000 subjects, the validation set includes 1784 sequences of 345 subjects and the testing set includes 24000 sequences of 6000 subjects.

B. Implementation Details

1) *Hyper-parameters:* (1) Follow the settings in [13], [23], we set the value of B (number of training samples in one iteration) as 64, 256 and 256 on CASIA-B [20], OU-MVLP [21] and GREW [22] datasets respectively. (2) The value of N (input frame number) and K (part division number) are set as 30 and 32. (3) The number of output channels for FC shown in Figure. 3 is set to 256, 512 and 512 for CASIA-B [20], OU-MVLP [21] and GREW [22] datasets respectively. (4) All MLPs follow: $FC(c, c/16) \rightarrow ReLU() \rightarrow FC(c/16, c)$. The two FCs in ATA are $FC(c, c/16)$ and $FC(c/16, c)$.

2) *Training Details:* (1) Each frame is aligned as [21] does, and we resize each frame to the size of 64×44 or 128×88 . For each input sequence, we follow the frame sampling strategy as [8] does. (2) We apply separate Batch All (BA_+) triplet loss to train our network. The batch size for training is noted as (p, k) , where p denotes the number of sampled subjects and k denotes the number of sampled sequences for each subject. Particularly, (p, k) is set to (8, 8) on CASIA-B and (32, 8) on OU-MVLP and GREW. (3) The backbone architecture on CASIA-B is given in Table. I. Since the data amount of OU-MVLP and GREW is much larger than that of CASIA-B, the numbers of output channels of each layer in Table. I are set to 64, 128, 256, 256 on OU-MVLP and GREW datasets, which follows the design in GaitSet [31]. (4) Totally, we train 120k iterations on CASIA-B and 250k iterations on OU-MVLP and GREW. Moreover, our model is optimized by Adam, and the learning rate is started to set as $1e-4$ and reduced to $1e-5$ at 150k iterations on OU-MVLP and GREW. We implement our models on Pytorch [58] platform and use four NVIDIA GeForce GTX 3090 GPUs to perform our experiments.

C. Comparison with the State-of-the-art Methods

CASIA-B. Table. II shows the comparison results between the proposed MCAT and current state-of-the-art methods in averaged rank-1 accuracies on CASIA-B dataset. Three walking conditions (NM, BG, CL) and 11 different camera views ($0^\circ - 180^\circ$) are considered into performance evaluation. Three notable conclusions are summarized as: (1) MCAT outperforms all other methods in mean accuracy comparisons under all cases, which demonstrates the robustness and advantages. (2) It is natural that recognition performances would oscillate under different camera viewpoints. However, compared with other SOTA approaches, MCAT achieves almost the lowest performance standard deviation across 11 views under all walking conditions, which proves the robustness against viewpoint variations. (3) MCAT also shows robustness to resolution variations of gait sequences. Under different resolution settings of three walking conditions, MCAT achieves better mean recognition accuracies over current methods, which reveals that MCAT could adapt to different resolutions flexibly. Based on that, we use resolution setting of 64×44 in the rest of this paper since it achieves better tradeoff between performance and computation cost.

Further, we draw the performance curves of the 11 views of CASIA-B in Figure. 7, which illustrates the accuracy fluctuations under cross-view scenarios. We find that: (1) All curves look like saddle-shape, which are roughly symmetric about the 90° view. This phenomenon reveals that sequences from symmetric views contain similar spatial-temporal information for recognition, which adheres to human intuitions. (2) Compared with the sequences from side view (90°) and front (0°) or back view (180°), sequences from the squint views (36° or 144°) achieve better performances, which may be attributed to the squint views incorporating rich visual clues from both side view and front or back view.

OU-MVLP. Table. III shows the comparison results between the proposed MCAT and current state-of-the-art methods in terms of averaged rank-1 accuracies on OU-MVLP. Our MCAT outperforms the existing methods under mean accuracy comparison, which proves the generalization capacity on a large-scale dataset. Particularly, though 3DLocal achieves competitive performance with MCAT under the setting of keeping invalid sequences, MCAT achieves much lower performance standard deviation than 3DLocal (0.9% with 2.0%), which demonstrates the stronger stability of viewpoint changes. Taking the performances under 0° and 180° as examples, MCAT marginally outperforms 3DLocal by 2.4% and 3.4% respectively. This phenomenon explains that MCAT has fewer preferences on certain camera viewpoints compared with current methods. Besides, by removing the invalid probe sequences, MCAT achieves much better accuracy compared with other methods.

GREW. Table. IV shows the comparison results between the proposed MCAT and current state-of-the-art methods. We can see sequences based method significantly outperforms Gait Energy Image (GEI) based method which indicates sequences based method has stronger ability to model the gait pattern in real scenarios. Compared to other temporal modeling methods,

TABLE II
AVERAGED RANK-1 ACCURACIES (%) ON CASIA-B, EXCLUDING IDENTICAL-VIEW CASES. STD DENOTES THE PERFORMANCE SAMPLE STANDARD DEVIATION ACROSS 11 VIEWS.

Gallery NM		Resolution	0 – 180°											Mean	Std
Probe		—	0°	18°	36°	54°	72°	90°	108°	126°	144°	162°	180°		
NM	GaitSet [31]	64 × 44	91.1	99.0	99.9	97.8	95.1	94.5	96.1	98.3	99.2	98.1	88.0	96.1	3.5
	GaitPart [8]	64 × 44	94.1	98.6	99.3	98.5	94.0	92.3	95.9	98.4	99.2	97.8	90.4	96.2	3.1
	GaitGL [13]	64 × 44	96.0	98.3	99.0	97.9	96.9	95.4	97.0	98.9	99.3	98.8	94.0	97.4	1.7
	3DLocal [40]	64 × 44	96.0	99.0	99.5	98.9	97.1	94.2	96.3	99.0	98.8	98.5	95.2	97.5	1.8
	GaitTransformer [41]	64 × 44	94.9	98.3	98.4	97.8	94.8	94.1	96.3	98.5	99.0	98.3	90.7	96.5	2.5
	Lagrange [59]	64 × 44	95.2	97.8	99.0	98.0	96.9	94.6	96.9	98.8	98.9	98.0	91.5	96.9	2.2
	STAR [42]	64 × 44	96.5	98.7	99.0	97.6	96.1	95.4	96.8	98.6	99.1	98.9	93.9	97.3	1.6
	GaitBase [43]	64 × 44	-	-	-	-	-	-	-	-	-	-	-	97.6	-
	MCAT (Ours)	64 × 44	97.7	99.3	99.4	99.1	97.3	96.1	98.5	99.7	99.7	99.2	96.9	98.5	1.2
	GLN [32]	128 × 88	93.2	99.3	99.5	98.7	96.1	95.6	97.2	98.1	99.3	98.6	90.1	96.9	3.0
	3DLocal [40]	128 × 88	97.8	99.4	99.7	99.3	97.5	96.0	98.3	99.1	99.9	99.2	94.6	98.3	1.7
	STAR [42]	128 × 88	95.8	98.9	99.0	98.0	96.0	94.4	96.8	98.9	99.3	99.4	94.4	97.4	1.8
	MCAT (Ours)	128 × 88	97.6	99.4	99.3	98.9	97.9	97.9	98.9	99.8	99.9	99.6	96.7	98.7	1.0
BG	GaitSet [31]	64 × 44	86.7	94.2	95.7	93.4	88.9	85.5	89.0	91.7	94.5	95.9	83.3	90.8	4.4
	GaitPart [8]	64 × 44	89.1	94.8	96.7	95.1	88.3	84.9	89.0	93.5	96.1	93.8	85.8	91.5	4.2
	GaitGL [13]	64 × 44	92.6	96.6	96.8	95.5	93.5	89.3	92.2	96.5	98.2	96.9	91.5	94.5	2.8
	3DLocal [40]	64 × 44	92.9	95.9	97.8	96.2	93.0	87.8	92.7	96.3	97.9	98.0	88.5	94.3	3.5
	GaitTransformer [41]	64 × 44	89.9	94.5	95.9	94.6	93.9	88.8	91.1	96.3	98.1	97.3	88.9	93.5	3.7
	Lagrange [59]	64 × 44	89.9	94.5	95.9	94.6	93.9	88.0	91.1	96.3	98.1	97.3	88.9	93.5	3.2
	STAR [42]	64 × 44	92.3	96.7	97.1	95.6	92.6	88.5	92.3	96.0	97.0	95.7	89.0	93.9	3.0
	GaitBase [43]	64 × 44	-	-	-	-	-	-	-	-	-	-	-	94.0	-
	MCAT (Ours)	64 × 44	94.6	97.5	97.0	95.7	92.0	90.2	91.9	96.2	97.9	97.2	92.5	94.8	2.7
	GLN [32]	128 × 88	91.1	97.7	97.8	95.2	92.5	91.2	92.4	96.0	97.5	95.0	88.1	94.0	3.2
	3DLocal [40]	128 × 88	94.7	98.7	98.8	97.5	93.3	91.7	92.8	96.5	98.1	97.3	90.7	95.5	2.9
	STAR [42]	128 × 88	93.6	98.0	98.3	96.1	93.9	91.7	94.8	97.6	98.2	97.5	91.8	95.6	2.4
	MCAT (Ours)	128 × 88	95.9	97.1	97.8	97.2	95.1	93.0	96.1	97.5	98.0	97.4	93.8	96.2	1.7
CL	GaitSet [31]	64 × 44	59.5	75.0	78.3	74.6	71.4	71.3	70.8	74.1	74.6	69.4	54.1	70.3	7.2
	GaitPart [8]	64 × 44	70.7	85.5	86.9	83.3	77.1	72.5	76.9	82.2	83.8	80.2	66.5	78.7	6.6
	GaitGL [13]	64 × 44	76.6	90.0	90.3	87.1	84.5	79.0	84.1	87.0	87.3	84.4	69.5	83.6	6.3
	3DLocal [40]	64 × 44	78.2	90.2	92.0	87.1	83.0	76.8	83.1	86.6	86.8	84.1	70.9	83.7	6.2
	GaitTransformer [41]	64 × 44	81.5	91.9	92.2	91.2	85.9	83.1	86.8	90.7	90.4	89.0	75.6	87.1	5.0
	Lagrange [59]	64 × 44	81.6	91.0	94.8	92.2	85.5	82.1	86.0	89.8	90.6	86.0	73.5	86.6	5.7
	STAR [42]	64 × 44	77.9	89.5	92.1	88.2	83.1	80.8	83.3	86.5	88.7	85.8	68.3	84.0	6.3
	GaitBase [43]	64 × 44	-	-	-	-	-	-	-	-	-	-	-	77.4	-
	MCAT (Ours)	64 × 44	78.5	90.5	91.6	86.9	84.4	80.8	83.3	87.5	88.0	85.0	73.0	84.5	5.5
	GLN [32]	128 × 88	70.6	82.4	85.2	82.7	79.2	76.4	76.2	78.9	77.9	78.7	64.3	77.5	5.8
	3DLocal [40]	128 × 88	78.5	88.9	91.0	89.2	83.7	80.5	83.2	84.3	87.9	87.1	74.7	84.5	5.0
	STAR [42]	128 × 88	77.4	91.0	92.9	89.9	86.2	81.9	87.0	92.4	94.2	90.0	74.7	87.1	6.2
	MCAT (Ours)	128 × 88	84.2	92.6	93.4	89.9	87.1	85.2	87.4	90.6	92.3	90.8	82.2	88.7	3.7

MCAT, which has a richer representation of temporal features, has a large margin in all of the test settings. MCAT achieves the best performances under all comparison settings, which proves the gait modeling capacity of MCAT under complex real-world scenarios.

D. Ablation Study

In order to evaluate the exact effectiveness of MCAT, ablation experiments are conducted on CASIA-B to study the proposed components.

Impact of Spatio-Temporal Modeling. The individual effects of spatial and temporal modeling are presented in Table. V. The baseline refers to the 4-layer CNN with a feature division, while using a BA+ loss for supervision. Several noteworthy observations can be summarized as: (1) Compared to spatial modeling network, i.e. GaitSet [31], our baseline achieves similar mean accuracy under three conditions (85.7% and 85.4%), which proves the competitive spatial learning capacity of them. However, with the utilization of MSTE, our method achieves significant accuracy improvement over GaitSet [31] (+3.9%), which indicates the superiority of modeling multi-

scale temporal context based on spatial feature extraction. (2) Compared with the multi-scale temporal modeling method, i.e., GaitPart, our method achieves higher performances when applying MSTE with ATA (+2.5%) and MSTE with SSFL (+2.7%), which verifies the effectiveness of adaptive temporal aggregation and salient spatial mining based on multi-scale temporal clues. (3) Applying both spatial and temporal modeling achieves the best results, which verifies the complementary properties provided by SSFL and ATA modules.

Effectiveness of Local and Global Relation Modeling. Table. VI investigates the effectiveness of the proposed local and global relation modeling strategies. In order to investigate the superiority of the proposed local relation modeling module, we use max pooling and attention [23] method for comparison. We find that, using an FC achieves the best performance over other methods, which proves its superiority for fusing multi-scale features locally. Therefore, we take an FC as local relation modeling in the final version. Further, local-with-global joint modeling achieves the best performance, which demonstrates the complementary properties introduced by local and global relation modelings.

TABLE III

AVERAGED RANK-1 ACCURACIES (%) ON OU-MVLP, EXCLUDING IDENTICAL-VIEW CASES. STD DENOTES THE PERFORMANCE SAMPLE STANDARD DEVIATION ACROSS 14 VIEWS. THE RESULTS IN THE FIRST 10 ROWS AND THE LAST 6 ROWS ARE CONDUCTED BY KEEPING OR REMOVING INVALID PROBE SEQUENCES THAT HAVE NO CORRESPONDING TARGETS IN THE GALLERY SET.

Method	Probe View														Mean	Std
	0°	15°	30°	45°	60°	75°	90°	180°	195°	210°	225°	240°	255°	270°		
GaitSet [31]	81.3	88.6	90.2	90.7	88.6	89.1	88.3	83.1	87.7	89.4	89.7	87.8	88.3	86.9	87.9	2.6
GaitPart [8]	82.6	88.9	90.8	91.0	89.7	89.9	89.5	85.2	88.1	90.0	90.1	89.0	89.1	88.2	88.7	2.3
GLN [32]	83.8	90.0	91.0	91.2	90.3	90.0	89.4	85.3	89.1	90.5	90.6	89.6	89.3	88.5	89.2	2.1
GaitGL [13]	84.9	90.2	91.1	91.5	91.1	90.8	90.3	88.5	88.6	90.3	90.4	89.6	89.5	88.8	89.7	1.7
3DLocal [40]	86.1	91.2	92.6	92.9	92.2	91.3	91.1	86.9	90.8	92.2	92.3	91.3	91.1	90.2	90.9	2.0
GaitTransformer [41]	87.9	91.3	91.6	91.7	91.6	91.3	91.1	90.3	90.4	90.8	91.0	90.6	90.3	90.0	90.7	1.0
Lagrange [59]	85.9	90.6	91.3	91.5	91.2	91.0	90.6	88.9	89.2	90.5	90.6	89.9	89.8	89.2	90.0	1.4
STAR [42]	85.5	90.0	91.4	91.6	90.5	90.7	90.2	88.0	88.5	90.5	90.7	89.7	89.7	88.9	89.7	1.5
GaitBase [43]	-	-	-	-	-	-	-	-	-	-	-	-	-	-	90.8	-
MCAT (Ours)	88.5	91.5	91.7	92.0	91.8	91.4	91.2	90.3	90.9	91.1	91.2	90.8	90.7	90.4	91.0	0.9
GaitSet [31]	84.5	93.3	96.7	96.6	93.5	95.3	94.2	87.0	92.5	96.0	96.0	93.0	94.3	92.7	93.3	3.5
GaitPart [8]	88.0	94.7	97.7	97.6	95.5	96.6	96.2	90.6	94.2	97.2	97.1	95.1	96.0	95.0	95.1	2.7
GLN [32]	89.3	95.8	97.9	97.8	96.0	96.7	96.1	90.7	95.3	97.7	97.5	95.7	96.2	95.3	95.6	2.5
GaitGL [13]	90.5	96.1	98.0	98.1	97.0	97.6	97.1	94.2	94.9	97.4	97.4	95.7	96.5	95.7	96.2	2.0
3DLocal [40]	-	-	-	-	-	-	-	-	-	-	-	-	-	-	96.5	-
MCAT (Ours)	94.3	97.5	98.7	98.7	97.7	98.3	98.1	96.1	97.3	98.3	98.3	97.1	97.8	97.4	97.5	1.2

TABLE IV

AVERAGED RANK-1, RANK-5, RANK-10 AND RANK-20 ACCURACIES (%) ON GREW, EXCLUDING IDENTICAL-VIEW CASES.

Method	Rank-1	Rank-5	Rank-10	Rank-20
GEINet [60]	6.8	13.4	17.0	21.0
TS-CNN [36]	13.6	24.6	30.2	37.0
GaitSet [31]	46.3	63.6	70.3	76.8
GaitPart [8]	44.0	60.7	67.3	73.5
MCAT (Ours)	50.6	65.9	71.9	76.9

TABLE V

STUDY OF THE EFFECTIVENESS OF MODULES IN MCAT ON CASIA-B IN TERMS OF AVERAGED RANK-1 ACCURACY (%). FOR THE SAKE OF SIMPLICITY, WE USE MSTE TO DENOTE MULTI-SCALE TEMPORAL EXTRACTION.

Model	Rank-1 Accuracy			
	NM	BG	CL	Mean
GaitSet [31]	96.1	90.8	70.3	85.7
GaitPart [8]	96.2	91.5	78.7	88.8
Ours				
Baseline	95.3	88.7	72.1	85.4
Baseline + MSTE	96.6	91.1	81.0	89.6
Baseline + MSTE + ATA	98.3	94.0	81.5	91.3
Baseline + MSTE + SSFL	97.7	93.0	83.8	91.5
MCAT	98.5	94.8	84.5	92.6

Comparison of Spatial Selection Strategies In order to investigate the effectiveness of our spatial learning module for supplementing corrupted spatial features, we conduct two more experiments for comparison: (1) We replace SSFL with a random frame selection to demonstrate that not each frame has good spatial features. (2) We set the number of selected parts as 1 in SSFL. In this situation, SSFL turns to be a frame-level feature selection instead of part-level feature selection.

As shown in Table. VII, we notice that: SSFL outperforms the other two strategies, which proves the spatial learning capability of our method. On one hand, random frame selection is probably incapable of obtaining high quality spatial features due to the randomness. On the other hand, although frame-level spatial selection achieves better performance than

TABLE VI

STUDY THE EFFECTIVENESS OF LOCAL AND GLOBAL RELATION MODELING ON CASIA-B IN TERMS OF AVERAGED RANK-1 ACCURACY (%).

Local Relation			Global Relation	Rank-1 Accuracy			
Max Pooling	FC	Attention		NM	BG	CL	Mean
✓				97.9	93.8	84.4	92.0
	✓			98.1	93.9	84.5	92.2
		✓		97.9	93.8	82.8	91.5
			✓	98.3	94.0	81.8	91.4
	✓		✓	98.5	94.8	84.5	92.6

TABLE VII

COMPARISONS OF SPATIAL SELECTION STRATEGIES ON CASIA-B IN TERMS OF AVERAGED RANK-1 ACCURACY (%).

Methods	Rank-1 Accuracy			
	NM	BG	CL	Mean
random frame	98.1	94.0	82.9	91.7
SSFL (frame-level)	98.5	94.5	83.7	92.2
SSFL	98.5	94.8	84.5	92.6

random frame selection, it still limits the diverse discriminative expression of local parts, especially considering the occlusion of motion and change of camera viewpoints. Compared to the above strategies, our SSFL extracts spatial clues in a fine-grained manner and utilizes the inherent motion characteristics to leverage rich visual clues across the sequence.

TABLE VIII

STUDY ON THE IMPACTS OF IMPORTANCE EVALUATION METHODS AND NUMBER OF SELECTED SPATIAL PARTS IN SSFL ON CASIA-B IN TERMS OF RANK-1 AVERAGED ACCURACY (%).

Method	Selected Groups	Rank-1 Accuracy			
MLP	1	98.1	93.6	83.5	91.7
MHSA	1	98.3	93.7	83.6	91.9
	2	98.3	93.8	83.5	91.8
	4	98.5	94.8	84.5	92.6
	8	98.5	94.2	83.6	92.1

Investigation on the impact factors of SSFL. Table VIII

investigates the impact factors in SSFL on CASIA-B dataset. Especially, the first experiment is conducted by using a MLP to produce the part scores of each frame locally, which can only select a group of salient parts. We can notice that: (1) MHSA outperforms MLP when selecting only one group of spatial parts, which illustrates the superiority of constructing the importance map globally. (2) When selecting more groups of spatial parts by MHSA, the recognition performance first improves continually, then drops. This phenomenon explains that the number of high quality salient parts in each sequence is limited, thus we may obtain low-quality parts by selecting redundant groups, which hurts the recognition performance. To achieve the best performance, we select 4 groups in our final version.

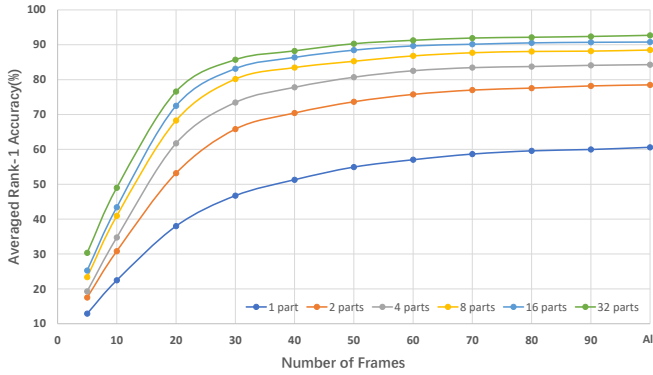


Fig. 8. Study on the impact of different part division numbers and frame numbers on CASIA-B [20] in terms of averaged rank-1 accuracy under NM, BG and CL conditions.

Ablation Study on Part Division Numbers and Frame Numbers. In order to investigate the effects of the part division number K and frame number N , we conduct ablation experiments with different number of K and N . Particularly, 32 is the largest number for K , since the output feature dimension is 32×22 . And the maximum N is set as the number of all frames in each sequence. As shown in Figure. 8, we can see that the accuracy improves continually with the increasing of number of parts and number of frames, which indicates that: (1) More fine-grained part division provides richer clues for modeling spatial local features, which further satisfies the diverse motion expression of different body parts. (2) More frames contain more abundant information for constructing temporal contextual communications, which enables the network to extract more discriminative temporal clues and mine more salient spatial parts.

Therefore, to achieve the best performance, we set the K as 32, and use all frames during test stage.

E. Practical Scenarios

In this section, we consider two new experimental settings, which are closer to real-world applications. (1) Because of the possible insufficiency of training data, models may be tested under unseen views in real life. (2) People may walk in arbitrary directions anytime and anywhere, thus one sequence may be composed of frames from different views.

Testing Under Unseen Views. As shown in Figure. 10, we consider two possible scenarios for testing the view generalization capacity of our method. Specially, scenario A corresponds to the case that the training dataset covers the view range in the test dataset, but does not include some certain views. In contrast, scenario B refers to the case that views in the training dataset and test dataset are in different ranges. Intuitively, scenario B is harder than scenario A.

As reported in Table. IX, the accuracy decreases under unseen views as expected. However, compared with the baseline, our method achieves stronger robustness against unseen scenarios, whose performances degrade 2.5% under scenario A and 8.1% under scenario B. These results demonstrate the spatial-temporal modeling and view generalization capacities of the proposed modules.

TABLE IX
PERFORMANCE COMPARISON UNDER UNSEEN VIEWS ON CASIA-B IN TERMS OF AVERAGED RANK-1 ACCURACY (%) UNDER ALL WALKING CONDITIONS, EXCLUDING IDENTICAL-VIEW CASES. PARTICULARLY, THE DEFAULT SETTING DENOTES THAT TEST VIEWS ARE IN ACCORDANCE WITH TRAIN VIEWS.

Method	Default Setting	Scenario A	Scenario B
Baseline	85.4	81.9	76.3
Ours	92.6	90.1	84.5

Sequences include different views As shown in Table. X, we conduct 5 more experiments that combine frames from different views into one sequence. Particularly, each sequence is composed of frames from a pair of views, which are defined by the view difference. Taking the view difference of 90° as an example, the corresponding pairs are: 0° & 90° , 18° & 108° , 36° & 126° , 54° & 144° , 72° & 162° , 90° & 180° . And for eliminating the effects of sequence length as far as possible, we only sample half of each sequence from each view. Particularly, the sequences in the probe set are composed of frames from different views, and the sequences in the gallery set are unchanged.

TABLE X
PERFORMANCE COMPARISON USING SEQUENCES INCLUDE DIFFERENT VIEWS ON CASIA-B IN TERMS OF AVERAGED RANK-1 ACCURACY (%) UNDER ALL WALKING CONDITIONS, EXCLUDING IDENTICAL-VIEW CASES.

View Difference	18°	36°	54°	72°	90°	Single View
Baseline	88.1	89.6	89.8	90.2	90.2	85.4
Ours	93.0	94.6	95.3	95.7	95.9	92.6

As given Table. X, our method marginally outperforms the baseline with all view pairs, which further proves the effectiveness of our method under novel scenarios. Interestingly, we find that: (1) Using frames from different views achieves higher performances than using frames from one single view, which reveals that richer clues could be obtained in different views. (2) Using frames from larger view differences could consistently achieve higher performances, which reflects that more complementary information is provided in larger view-difference pairs.

Consequently, we argue that combine frames from different views could facilitate gait recognition in real-world scenarios effectively.

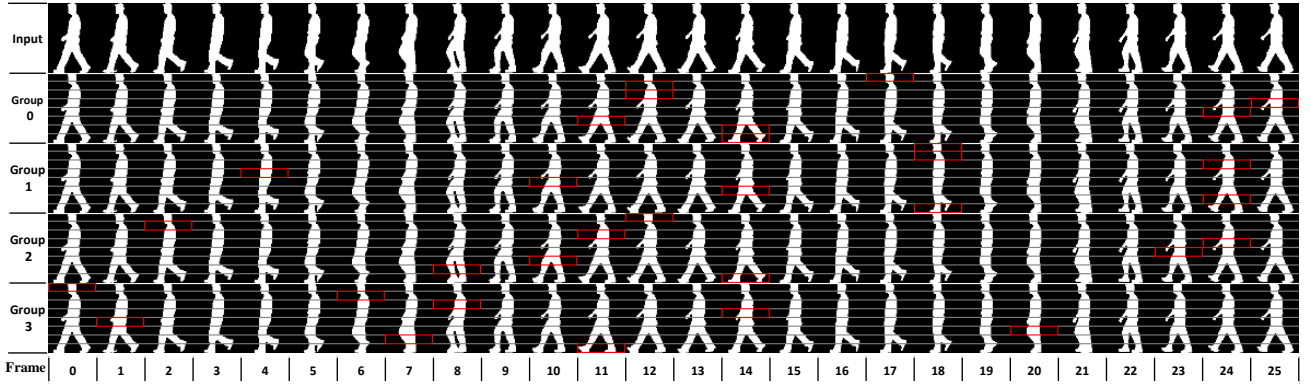


Fig. 9. Illustration of spatial salient feature learning. We select four groups of salient local parts. The red boxes indicate selected parts.

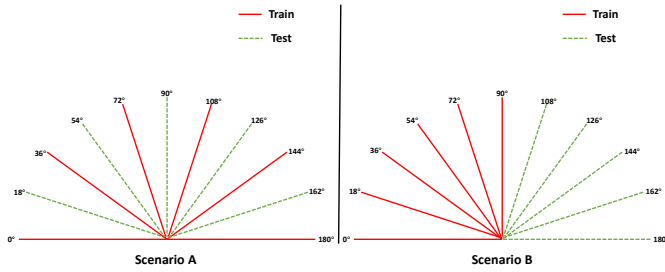


Fig. 10. Illustration of testing models under unseen views.

Salient Spatial Part Selection. In order to better understand the positive effects of SSFL, we give an example in Figure. 9, where we set the number of selected parts as 8 for better visualization. We can notice that: (1) Directly perceived through the senses, SSFL tends to select parts with clear representation and complete appearance features, which are not affected by body overlaps and clothing occlusions, e.g., from frame 8 to frame 14 and from frame 23 to frame 25. In contrast, frames with body overlaps are less selected, e.g., from frame 3 to frame 7 and from frame 19 to frame 21. (2) Various groups select a particular body part from different frames, showcasing the diverse focus in several aspects of MHSA. For example, the head in group 1 is selected from frame 18 while in group 3 is selected from frame 0.

In this way, we can obtain high quality spatial features, which both remedies the negative influences caused by temporal operations and enhances the robustness of our network against occlusion variations.

Feature Distribution. We choose ten identities from CASIA-B test dataset to visualize feature distributions by t-SNE [61]. Comparing the feature distributions of baseline and our method, we notice that, in Figure. 11(a), the feature distributions of different subjects are closer to each other thus identities are harder to distinguish. Differently, in Figure. 11(b), the feature distributions of different subjects are more scattered to each other thus identities are more distinguishable, which proves the discriminant feature learning ability of our method.

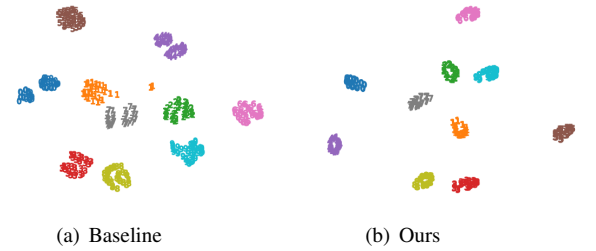


Fig. 11. tSNE visualization examples of the baseline and our proposed model on CASIA-B test dataset. Different numbers with different colors indicate different identities. Best viewed with zooming in.

V. CONCLUSION

In this paper, we propose a multi-scale context-aware network with transformer (MCAT) for gait recognition. MCAT extracts temporal features with multiple scales and captures salient spatial clues for achieving strong spatio-temporal modeling ability. Specifically, diverse temporal features in three scales are introduced in MCAT, and local-to-global temporal relations are considered based on these temporal information for adaptive temporal aggregation. Besides, discriminative spatial parts are selected across the sequence to remedy the spatial feature corruption. Extensive experiments on three public datasets verify the superiority and the real-world application potentials of our method. In addition, we argue that the insights of learning spatial and temporal features in a supplementary manner could be also applied in other human action-related tasks, e.g., video-based person re-identification. We leave this for future work.

REFERENCES

- [1] P. K. Larsen, E. B. Simonsen, and N. Lynnerup, "Gait analysis in forensic medicine," *Journal of forensic sciences*, vol. 53, no. 5, pp. 1149–1153, 2008.
- [2] I. Bouchrika, M. Goffredo, J. Carter, and M. Nixon, "On using gait in forensic biometrics," *Journal of forensic sciences*, vol. 56, no. 4, pp. 882–889, 2011.
- [3] S. X. Yang, P. K. Larsen, T. Alkjær, N. Lynnerup, and E. B. Simonsen, "Influence of velocity on variability in gait kinematics: implications for recognition in forensic science," *Journal of forensic sciences*, vol. 59, no. 5, pp. 1242–1247, 2014.

- [4] S. X. Yang, P. K. Larsen, T. Alkjær, E. B. Simonsen, and N. Lynnerup, "Variability and similarity of gait as evaluated by joint angles: implications for forensic gait analysis," *Journal of forensic sciences*, vol. 59, no. 2, pp. 494–504, 2014.
- [5] I. Macoveciuc, C. J. Rando, and H. Borrión, "Forensic gait analysis and recognition: standards of evidence admissibility," *Journal of forensic sciences*, vol. 64, no. 5, pp. 1294–1303, 2019.
- [6] M. Balazia and K. N. Platanotis, "Human gait recognition from motion capture data in signature poses," *IET Biometrics*, vol. 6, no. 2, pp. 129–137, 2017.
- [7] G. Premalatha and P. V. Chandramani, "Improved gait recognition through gait energy image partitioning," *Computational Intelligence*, vol. 36, no. 3, pp. 1261–1274, 2020.
- [8] C. Fan, Y. Peng, C. Cao, X. Liu, S. Hou, J. Chi, Y. Huang, Q. Li, and Z. He, "Gaitpart: Temporal part-based model for gait recognition," *CVPR*, pp. 14 225–14 233, 2020.
- [9] H. Wu, J. Tian, Y. Fu, B. Li, and X. Li, "Condition-aware comparison scheme for gait recognition," *IEEE Transactions on Image Processing*, 2020.
- [10] Y. Zhang, Y. Huang, S. Yu, and L. Wang, "Cross-view gait recognition by discriminative feature learning," *TIP*, vol. 29, pp. 1001–1015, 2019.
- [11] Z. Zhang, L. Tran, F. Liu, and X. Liu, "On learning disentangled representations for gait recognition," *IEEE Transactions on Pattern Analysis and Machine Intelligence*, 2020.
- [12] B. Lin, S. Zhang, and F. Bao, "Gait recognition with multiple-temporal-scale 3d convolutional neural network," *ACMMM*, pp. 3054–3062, 2020.
- [13] B. Lin, S. Zhang, and X. Yu, "Gait recognition via effective global-local feature representation and local temporal aggregation," in *Proceedings of the IEEE/CVF International Conference on Computer Vision*, 2021, pp. 14 648–14 656.
- [14] P. Zhang, X. Dai, J. Yang, B. Xiao, L. Yuan, L. Zhang, and J. Gao, "Multi-scale vision longformer: A new vision transformer for high-resolution image encoding," in *Proceedings of the IEEE/CVF international conference on computer vision*, 2021, pp. 2998–3008.
- [15] C.-F. R. Chen, Q. Fan, and R. Panda, "Crossvit: Cross-attention multi-scale vision transformer for image classification," in *Proceedings of the IEEE/CVF international conference on computer vision*, 2021, pp. 357–366.
- [16] A. Dosovitskiy, L. Beyer, A. Kolesnikov, D. Weissenborn, X. Zhai, T. Unterthiner, M. Dehghani, M. Minderer, G. Heigold, S. Gelly *et al.*, "An image is worth 16x16 words: Transformers for image recognition at scale," *arXiv preprint arXiv:2010.11929*, 2020.
- [17] H. Liu, Y. Liu, Y. Chen, C. Yuan, B. Li, and W. Hu, "Transkeleton: Hierarchical spatial-temporal transformer for skeleton-based action recognition," *IEEE Transactions on Circuits and Systems for Video Technology*, 2023.
- [18] X. Zhu, Y. Zhou, D. Wang, W. Ouyang, and R. Su, "Mlst-former: Multi-level spatial-temporal transformer for group activity recognition," *IEEE Transactions on Circuits and Systems for Video Technology*, 2022.
- [19] A. Vaswani, N. Shazeer, N. Parmar, J. Uszkoreit, L. Jones, A. N. Gomez, Ł. Kaiser, and I. Polosukhin, "Attention is all you need," *Advances in neural information processing systems*, vol. 30, 2017.
- [20] S. Yu, D. Tan, and T. Tan, "A framework for evaluating the effect of view angle, clothing and carrying condition on gait recognition," *ICPR*, vol. 4, pp. 441–444, 2006.
- [21] N. Takemura, Y. Makihara, D. Muramatsu, T. Echigo, and Y. Yagi, "Multi-view large population gait dataset and its performance evaluation for cross-view gait recognition," *IPSI Transactions on Computer Vision and Applications*, vol. 10, no. 1, p. 4, 2018.
- [22] Z. Zhu, X. Guo, T. Yang, J. Huang, J. Deng, G. Huang, D. Du, J. Lu, and J. Zhou, "Gait recognition in the wild: A benchmark," in *Proceedings of the IEEE/CVF International Conference on Computer Vision*, 2021, pp. 14 789–14 799.
- [23] X. Huang, D. Zhu, H. Wang, X. Wang, B. Yang, B. He, W. Liu, and B. Feng, "Context-sensitive temporal feature learning for gait recognition," in *Proceedings of the IEEE/CVF International Conference on Computer Vision*, 2021, pp. 12 909–12 918.
- [24] R. Liao, C. Cao, E. B. Garcia, S. Yu, and Y. Huang, "Pose-based temporal-spatial network (ptsn) for gait recognition with carrying and clothing variations," *Chinese conference on biometric recognition*, pp. 474–483, 2017.
- [25] R. Liao, C. Cao, E. B. Garcia, S. Yu, and Y. Huang, "Pose-based temporal-spatial network (ptsn) for gait recognition with carrying and clothing variations," *Chinese conference on biometric recognition*, pp. 474–483, 2017.
- [26] T. Teepe, A. Khan, J. Gilg, F. Herzog, S. Hörmann, and G. Rigoll, "Gait-graph: Graph convolutional network for skeleton-based gait recognition," *arXiv preprint arXiv:2101.11228*, 2021.
- [27] X. Huang, X. Wang, Z. Jin, B. Yang, B. He, B. Feng, and W. Liu, "Condition-adaptive graph convolution learning for skeleton-based gait recognition," *IEEE Transactions on Image Processing*, vol. 32, pp. 4773–4784, 2023.
- [28] Z. Cao, G. Hidalgo, T. Simon, S.-E. Wei, and Y. Sheikh, "Openpose: realtime multi-person 2d pose estimation using part affinity fields," *IEEE transactions on pattern analysis and machine intelligence*, vol. 43, no. 1, pp. 172–186, 2019.
- [29] K. Sun, B. Xiao, D. Liu, and J. Wang, "Deep high-resolution representation learning for human pose estimation," *Proceedings of the IEEE/CVF Conference on Computer Vision and Pattern Recognition*, pp. 5693–5703, 2019.
- [30] Z. Cao, T. Simon, S.-E. Wei, and Y. Sheikh, "Realtime multi-person 2d pose estimation using part affinity fields," *Proceedings of the IEEE conference on computer vision and pattern recognition*, pp. 7291–7299, 2017.
- [31] H. Chao, K. Wang, Y. He, J. Zhang, and J. Feng, "Gaitset: Cross-view gait recognition through utilizing gait as a deep set," *IEEE Transactions on Pattern Analysis and Machine Intelligence*, 2021.
- [32] S. Hou, C. Cao, X. Liu, and Y. Huang, "Gait lateral network: Learning discriminative and compact representations for gait recognition," *European Conference on Computer Vision*, pp. 382–398, 2020.
- [33] T. Wolf, M. Babae, and G. Rigoll, "Multi-view gait recognition using 3d convolutional neural networks," *ICIP*, pp. 4165–4169, 2016.
- [34] J. Han and B. Bhanu, "Individual recognition using gait energy image," *IEEE transactions on pattern analysis and machine intelligence*, vol. 28, no. 2, pp. 316–322, 2005.
- [35] Y. He, J. Zhang, H. Shan, and L. Wang, "Multi-task gans for view-specific feature learning in gait recognition," *IEEE Transactions on Information Forensics and Security*, vol. 14, no. 1, pp. 102–113, 2018.
- [36] Z. Wu, Y. Huang, L. Wang, X. Wang, and T. Tan, "A comprehensive study on cross-view gait based human identification with deep cnns," *IEEE transactions on pattern analysis and machine intelligence*, vol. 39, no. 2, pp. 209–226, 2016.
- [37] M. Hu, Y. Wang, Z. Zhang, J. J. Little, and D. Huang, "View-invariant discriminative projection for multi-view gait-based human identification," *IEEE Transactions on Information Forensics and Security*, vol. 8, no. 12, pp. 2034–2045, 2013.
- [38] X. Li, Y. Makihara, C. Xu, Y. Yagi, and M. Ren, "Gait recognition via semi-supervised disentangled representation learning to identity and covariate features," *CVPR*, pp. 13 309–13 319, 2020.
- [39] C. Xu, Y. Makihara, X. Li, Y. Yagi, and J. Lu, "Cross-view gait recognition using pairwise spatial transformer networks," *IEEE Transactions on Circuits and Systems for Video Technology*, vol. 31, no. 1, pp. 260–274, 2020.
- [40] Z. Huang, D. Xue, X. Shen, X. Tian, H. Li, J. Huang, and X.-S. Hua, "3d local convolutional neural networks for gait recognition," in *Proceedings of the IEEE/CVF International Conference on Computer Vision*, 2021, pp. 14 920–14 929.
- [41] Y. Cui and Y. Kang, "Gaittransformer: Multiple-temporal-scale transformer for cross-view gait recognition," in *2022 IEEE International Conference on Multimedia and Expo (ICME)*. IEEE, 2022, pp. 1–6.
- [42] X. Huang, X. Wang, B. He, S. He, W. Liu, and B. Feng, "Star: Spatio-temporal augmented relation network for gait recognition," *IEEE Transactions on Biometrics, Behavior, and Identity Science*, vol. 5, no. 1, pp. 115–125, 2023.
- [43] C. Fan, J. Liang, C. Shen, S. Hou, Y. Huang, and S. Yu, "Opengait: Revisiting gait recognition towards better practicality," in *Proceedings of the IEEE/CVF Conference on Computer Vision and Pattern Recognition*, 2023, pp. 9707–9716.
- [44] Z. Huang, D. Xue, X. Shen, X. Tian, H. Li, J. Huang, and X.-S. Hua, "3d local convolutional neural networks for gait recognition," in *Proceedings of the IEEE/CVF International Conference on Computer Vision*, 2021, pp. 14 920–14 929.
- [45] A. Dosovitskiy, L. Beyer, A. Kolesnikov, D. Weissenborn, X. Zhai, T. Unterthiner, M. Dehghani, M. Minderer, G. Heigold, S. Gelly *et al.*, "An image is worth 16x16 words: Transformers for image recognition at scale," *arXiv preprint arXiv:2010.11929*, 2020.
- [46] Z. Liu, Y. Lin, Y. Cao, H. Hu, Y. Wei, Z. Zhang, S. Lin, and B. Guo, "Swin transformer: Hierarchical vision transformer using shifted windows," in *Proceedings of the IEEE/CVF International Conference on Computer Vision*, 2021, pp. 10 012–10 022.

- [47] J. Zhao, H. Wang, Y. Zhou, R. Yao, S. Chen, and A. El Saddik, "Spatial-channel enhanced transformer for visible-infrared person re-identification," *IEEE Transactions on Multimedia*, 2022.
- [48] Z. Tang, R. Zhang, Z. Peng, J. Chen, and L. Lin, "Multi-stage spatio-temporal aggregation transformer for video person re-identification," *IEEE Transactions on Multimedia*, 2022.
- [49] Y. Zhang, Y. Pan, T. Yao, R. Huang, T. Mei, and C.-W. Chen, "End-to-end video scene graph generation with temporal propagation transformer," *IEEE Transactions on Multimedia*, 2023.
- [50] A. Arnab, M. Dehghani, G. Heigold, C. Sun, M. Lučić, and C. Schmid, "Vivit: A video vision transformer," in *Proceedings of the IEEE/CVF International Conference on Computer Vision*, 2021, pp. 6836–6846.
- [51] Y. Zhang, X. Li, C. Liu, B. Shuai, Y. Zhu, B. Brattoli, H. Chen, I. Marsic, and J. Tighe, "Vidtr: Video transformer without convolutions," in *Proceedings of the IEEE/CVF International Conference on Computer Vision*, 2021, pp. 13 577–13 587.
- [52] X. Gu, H. Chang, B. Ma, H. Zhang, and X. Chen, "Appearance-preserving 3d convolution for video-based person re-identification," *European Conference on Computer Vision*, pp. 228–243, 2020.
- [53] G. Chen, Y. Rao, J. Lu, and J. Zhou, "Temporal coherence or temporal motion: Which is more critical for video-based person re-identification," *European Conference on Computer Vision*, pp. 660–676, 2020.
- [54] X. Chu, Z. Tian, B. Zhang, X. Wang, X. Wei, H. Xia, and C. Shen, "Conditional positional encodings for vision transformers," *arXiv preprint arXiv:2102.10882*, 2021.
- [55] S. N. Gowda, M. Rohrbach, and L. Sevilla-Lara, "Smart frame selection for action recognition," *arXiv preprint arXiv:2012.10671*, 2020.
- [56] O. Köpüklü, X. Wei, and G. Rigoll, "You only watch once: A unified cnn architecture for real-time spatiotemporal action localization," *arXiv preprint arXiv:1911.06644*, 2019.
- [57] A. Hermans, L. Beyer, and B. Leibe, "In defense of the triplet loss for person re-identification," *arXiv preprint arXiv:1703.07737*, 2017.
- [58] A. Paszke, S. Gross, S. Chintala, G. Chanan, E. Yang, Z. DeVito, Z. Lin, A. Desmaison, L. Antiga, and A. Lerer, "Automatic differentiation in pytorch," *NIPS Workshops*, 2017.
- [59] T. Chai, A. Li, S. Zhang, Z. Li, and Y. Wang, "Lagrange motion analysis and view embeddings for improved gait recognition," in *Proceedings of the IEEE/CVF Conference on Computer Vision and Pattern Recognition*, 2022, pp. 20 249–20 258.
- [60] K. Shiraga, Y. Makihara, D. Muramatsu, T. Echigo, and Y. Yagi, "Geinet: View-invariant gait recognition using a convolutional neural network," in *2016 international conference on biometrics (ICB)*. IEEE, 2016, pp. 1–8.
- [61] L. Van der Maaten and G. Hinton, "Visualizing data using t-sne," *Journal of machine learning research*, vol. 9, no. 11, 2008.



Duowang Zhu received the B.S. degree in School of Electronic Information and Communications from Huazhong University of Science and Technology (HUST), Wuhan, China, in 2020. Now, he is pursuing the M.S. degree in School of Electronic Information and Communications from Huazhong University of Science and Technology (HUST), Wuhan, China. His current research areas include computer vision and machine learning.



Xiaohu Huang received the B.S. degree in School of Electronic Information and Communications from Huazhong University of Science and Technology (HUST), Wuhan, China, in 2020. Now, he is pursuing the M.S. degree in School of Electronic Information and Communications from Huazhong University of Science and Technology (HUST), Wuhan, China. His current research areas include computer vision and machine learning.



Xinggong Wang (M'17) received the B.S. and Ph.D. degrees in Electronics and Information Engineering from Huazhong University of Science and Technology (HUST), Wuhan, China, in 2009 and 2014, respectively. He is currently an Associate Professor with the School of Electronic Information and Communications, HUST. His research interests include computer vision and machine learning. He services as associate editors for Pattern Recognition and Image and Vision Computing journals and an editorial board member of Electronics journal.



Bo Yang received the Master degree in School of mathematics and statistics from Wuhan University, Wuhan, China. He is currently the senior engineer of Wuhan FiberHome Digital Technology Co., Ltd. His research interests include computer vision and data mining.



Botao He received the Ph.D. degree in School of Optical and Electronic Information from Huazhong University of Science and Technology (HUST), Wuhan, China. He is currently the deputy general manager of CICT Mobile Communication Technology Company Ltd.. His research interests include computer vision and data mining.



Wenyu Liu (SM'15) received the B.S. degree in Computer Science from Tsinghua University, Beijing, China, in 1986, and the M.S. and Ph.D. degrees, both in Electronics and Information Engineering, from Huazhong University of Science and Technology (HUST), Wuhan, China, in 1991 and 2001, respectively. He is now a professor and associate dean of the School of Electronic Information and Communications, HUST. His current research areas include computer vision, multimedia, and machine learning.



Bin Feng received the B.S. and Ph.D. degrees in School of Electronics and Information Engineering from Huazhong University of Science and Technology (HUST), Wuhan, China, in 2001 and 2006, respectively. He is currently an Associate Professor with the School of Electronic Information and Communications, HUST. His research interests include computer vision and intelligent video analysis.